Platinum chemotherapy induces lymphangiogenesis to prime tissues for tumor metastasis

Alexandra R. Harris[2,4], Mohammad S. Azimi[3], Robert Cornelison[2,4], Francesca N. Azar[5], Danielle C. Llaneza[2], Maura Belanger[6], Alexander Mathew[3], Svyatoslav Tkachenko[7], Savieay Esparza[1], Matthew J. Perez[3], Claire Buchta Rosean[5], Raegan R. Bostic[5], R. Chase Cornelison[1], Kinsley M. Tate[1], Shayn M. Peirce-Cottler[3], Cherie Paquette[8,9], Anne Mills[4], Charles N. Landen[2], Jeff Saucerman[3], Patrick M. Dillon[10], Rebecca R. Pompano[6], Melanie A. Rutkowski[5], and Jennifer M. Munson [1,3] *

[1]Department of Biomedical Engineering & Mechanics, Virginia Tech-Wake Forest School of Biomedical Engineering & Sciences, Blacksburg, VA

[2]Department of Obstetrics and Gynecology, Gynecologic Oncology Division, University of Virginia, Charlottesville, VA

[3]Department of Biomedical Engineering, University of Virginia

[4]Department of Pathology, University of Virginia

[5]Department of Microbiology, Immunology, and Cancer Biology, University of Virginia

[6]Department of Chemistry, University of Virginia

[7]Lerner Research Institute, 9500 Euclid Avenue, JJN3-01, Cleveland, Ohio

[8]Department of Pathology and Laboratory Medicine, Brown University

[9]Department of Pathology and Laboratory Medicine, Women & Infants Hospital of Rhode Island

[10]Department of Hematology and Oncology, University of Virginia

*Correspondence addressed to:
Jennifer M Munson
Assistant Professor
Department of Biomedical Engineering & Mechanics
Virginia Polytechnic Institute and State University
349 Kelly Hall
325 Stanger Street
Blacksburg, VA 24061
Jm4kt@vt.edu
(540)-231-7896
@MunsonOEL

Abstract

Chemotherapy has been used to inhibit cancer growth for decades, but emerging evidence shows it can affect the tumor stroma unintentionally promoting cancer malignancy. After treatment of primary tumors, remaining drug drains via lymphatics. Though all drugs interact with the lymphatics, we know little of their impact on them. Here, we show a previously unknown effect of platinums, a widely used chemotherapeutic, to directly induce systemic VEGFR3-dependent lymphangiogenesis. These changes are dose-dependent, long-lasting, and occur in healthy and cancerous tissue in multiple mouse models of breast cancer. We saw similar effects in human ovarian and breast cancer patients whose treatment regimens included platinums. Carboplatin treatment results in lymphatic hyperplasia and secretion of pro-chemotactic factors in lymph nodes. Carboplatin treatment of healthy mice prior to mammary tumor inoculation increases cancer metastasis. These findings have broad-reaching implications for cancer patients receiving platinums and support the inclusion of anti-VEGFR3 therapy into treatment regimens.

Keywords:

Platinum, chemotherapy, lymphangiogenesis, metastasis, breast cancer, ovarian cancer

Summary Platinum chemotherapy induces lymphangiogenesis priming tissues for metastasis of breast cancer. Inhibition of VEGFR3 via antibody blockade can reverse these effects.

Introduction

Over 650,000 cancer patients receive chemotherapy in the United States every year, with platinums, taxanes, and anthracyclines representing the most common classes of drugs (*1*). Unfortunately, many of these patients suffer recurrence. In breast cancer, the second most common cause of cancer death in women in the US, mortality results from metastasis rather than primary tumor growth (*2*). Ovarian cancer is similarly deadly due to dissemination of tumor rather than initial growth (*3*). Despite the centrality of metastasis to patient outcomes, it remains unclear why tumors that appear to be controlled or even cleared by initial chemotherapy later recur.

Chemotherapeutic drugs enter the tumor via blood vasculature and drain through the stroma toward peritumoral lymphatics. Similarly, tumor cells metastasize from carcinomas primarily via the lymphatics and downstream lymph nodes (*4*). Thus, the lymphatics represent a point of access for both tumor cells and chemotherapies to the rest of the body. Enlargement, sprouting, and proliferation of lymphatic vessels at both the primary tumor site (*5*, *6*) and metastatic sites (*7*) are associated with increased cancer growth, metastasis, and poor prognosis (*8*). Treatment of lymphangiogenic tumors with inhibitors of VEGF Receptor 3 (VEGFR3), which targets lymphatic endothelial cells (LECs), inhibits systemic metastasis (*9*, *10*).

Although chemotherapies pass through lymphatics, thus interacting with these gatekeeping vessels, little information is available on how chemotherapies affect them (*9*, *10*). Although one class of chemotherapy – taxanes – was shown to induce lymphangiogenesis in mice (*10*), here we examine how the other major classes of chemotherapy impact the lymphatics, with an emphasis on platinum chemotherapy. Platinum agents are some of the most commonly used chemotherapies in the United States and are currently administered to treat a variety of cancers (*11*). Thus, we aimed to understand chemotherapeutic effects on the lymphatics.

Results

Lymphatic endothelial cells respond to platinum chemotherapy

We treated monolayers of human LECs with low doses of docetaxel, doxorubicin, or carboplatin. Breakdown of LEC junctions is associated with vessel permeability, enhancing opportunities for tumor cells to intravasate (*12*). We observed gaps in LECs treated with carboplatin (**Fig. 1A,B**), but not with doxorubicin or docetaxel (**Fig. S1A,B**). Treatment with other platinum agents (cisplatin and oxaliplatin) showed similar phenotypes (**Fig. S1C,D**). VEGFR3 activation can lead to phenotypic changes in LEC junctions (*13*), and we saw increased phosphorylated VEGFR3 on carboplatin-treated LECs (**Fig. 1C**).

Cellular adhesion molecules on LECs facilitate immune cell trafficking but are hijacked by tumor cells entering lymphatic vessels (*13*). LEC monolayers treated with carboplatin displayed higher numbers of ICAM1+ cells in hotspot regions compared to vehicle (**Fig. 1D,E**). Interestingly, platinum treatment (24h) did not diminish viability (**Fig. 1F**); in fact, it induced proliferation, a necessary precursor for *in vivo* lymphangiogenesis (**Fig. 1G, S1E,F**). Platinums were the only class of chemotherapy tested that induced significant proliferation in LECs (**Fig. 1H**). Together, these data suggest that platinum chemotherapy acts directly on LECs to induce phenotypes indicative of lymphangiogenesis.

Gene set enrichment analysis of microarray data of treated LECs showed upregulated proliferation, survival, and neovascularization pathways (**Fig. 1I, Table S1**). Carboplatin induced activation of the pro-survival and proliferation pathways MAPK, JAK-STAT, PI3K/AKT, RAS, and HIF1-α signaling in LECs. Induction of these pathways, paired with increased expression of genes such as *MTOR*, *INOS*, *ANGPT1*, *CMYC*, *PI3K*, and others, may suggest platinums are activating growth factor signaling in LECs in response to cellular stress. Reverse phase protein array (RPPA) and pathway analysis indicated similar pathway upregulation, pointing to signaling via FGFR, VEGFR, and EGFR families **(Table S2**). Other enriched pathways included those governing cellular adhesion molecules, GAP junctions, and chemokine signaling, all important in LEC activation. Pathway enrichment analysis of the top upregulated microRNAs (9 in total, >2-fold increase in expression) showed similar pathway activation (**Table S3**).

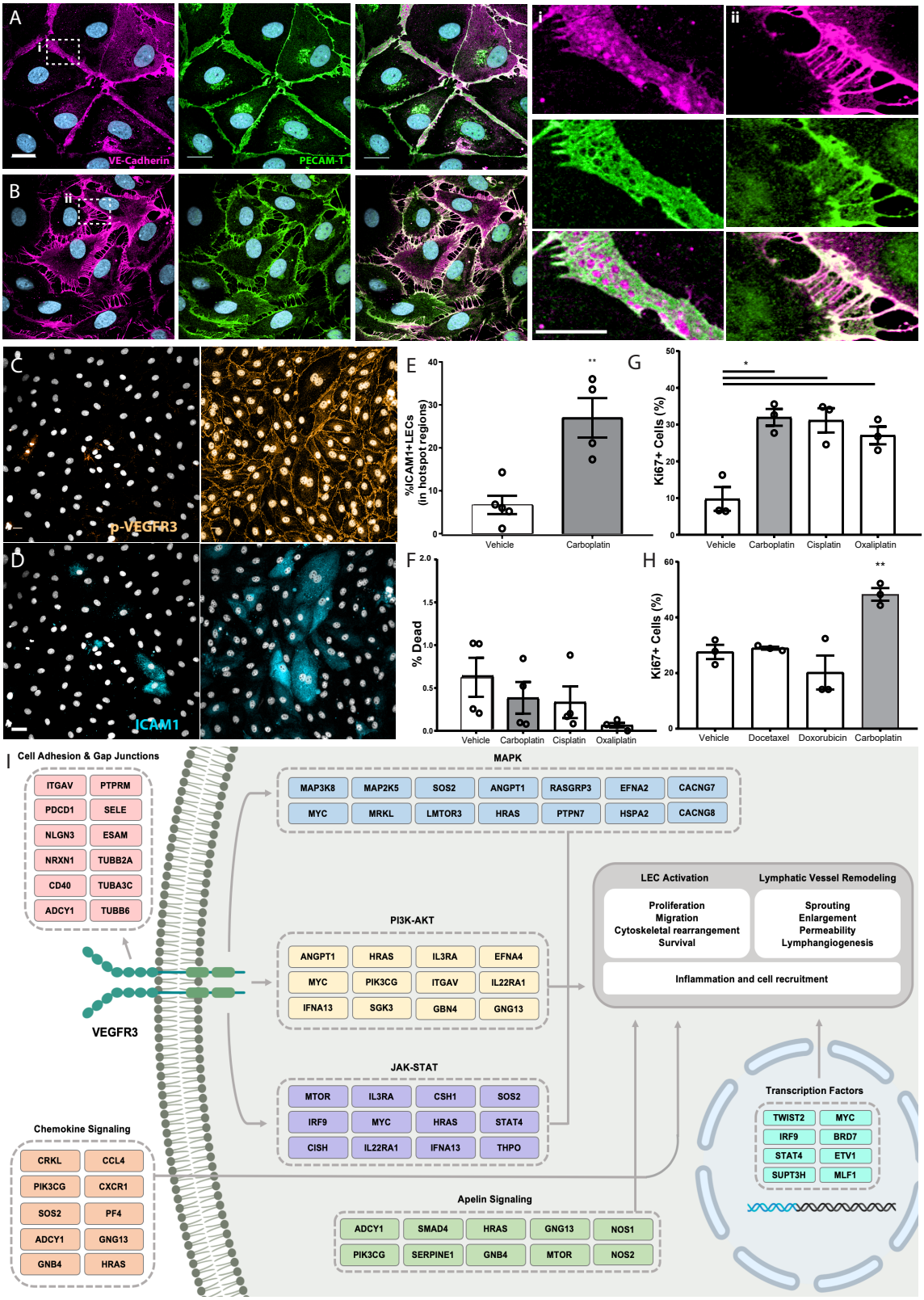
A
VE-Cadherin
PECAM-1
B
i
ii
C
p-VEGFR3
D
ICAM1
E
%ICAM1+LECs (in hotspot regions)
Vehicle
Carboplatin
F
% Dead
Vehicle
Carboplatin
Cisplatin
Oxaliplatin
G
Ki67+ Cells (%)
Vehicle
Carboplatin
Cisplatin
Oxaliplatin
H
Ki67+ Cells (%)
Vehicle
Docetaxel
Doxorubicin
Carboplatin
I
Cell Adhesion & Gap Junctions
ITGAV
PTPRM
PDCD1
SELE
NLGN3
ESAM
NRXN1
TUBB2A
CD40
TUBA3C
ADCY1
TUBB6
VEGFR3
MAPK
MAP3K8
MAP2K5
SOS2
ANGPT1
RASGRP3
EFNA2
CACNG7
MYC
MRKL
LMTOR3
HRAS
PTPN7
HSPA2
CACNG8
PI3K-AKT
ANGPT1
HRAS
IL3RA
EFNA4
MYC
PIK3CG
ITGAV
IL22RA1
IFNA13
SGK3
GBN4
GNG13
JAK-STAT
MTOR
IL3RA
CSH1
SOS2
IRF9
MYC
HRAS
STAT4
CISH
IL22RA1
IFNA13
THPO
LEC Activation
Proliferation
Migration
Cytoskeletal rearrangement
Survival
Lymphatic Vessel Remodeling
Sprouting
Enlargement
Permeability
Lymphangiogenesis
Inflammation and cell recruitment
Transcription Factors
TWIST2
MYC
IRF9
BRD7
STAT4
ETV1
SUPT3H
MLF1
Chemokine Signaling
CRKL
CCL4
PIK3CG
CXCR1
SOS2
PF4
ADCY1
GNG13
GNB4
HRAS
Apelin Signaling
ADCY1
SMAD4
HRAS
GNG13
NOS1
PIK3CG
SERPINE1
GNB4
MTOR
NOS2

Figure 1: Lymphatic endothelial cell (LEC) monolayers are activated by carboplatin (**A)** Untreated human LECs in monolayer culture; VE-cadherin (magenta) and PECAM-1 (green) with DAPI (gray-blue) for nuclei (scale bar=25µm) with (i) high magnification image cell-cell junction. **(B)** Human LEC monolayer treated with 1µM carboplatin with (ii) high magnification image of cell-cell junction. **(C)** Representative images of LECs after vehicle (*left*) or platinum chemotherapy (*right*) nuclei (DAPI, gray) and phospho-VEGFR3 (orange). **(D)** Representative images of LECs nuclei (DAPI, gray) and ICAM1 (cyan). Scale bar=250µm. **(E)** Percent ICAM1+ LECs in hotspot regions. **(F)** Percent dead cells per field after 48h of platinum agent (1µM) assessed by amine-based fluorescent reactive dye. **(G)** Percent proliferating cells per field by Ki67 positivity after 6h in culture with platinum agents (1 µM). **(H)** Percent proliferating cells per field by Ki67 positivity after 6h in culture with chemotherapeutic agents (1 µM). Each data set represents a minimum of three biological replicates. *$p<0.05$, **$p<0.01$. **(I)** Proposed mechanism generated from pathways enriched in LECs after *in vitro* treatment with carboplatin compared to vehicle-treated control. Gene members of each pathway were grouped reflecting their functional role in the cell.

Platinum chemotherapy induces dose-dependent and sustained lymphangiogenesis in healthy murine, rat, and human tissues

Building on these *in vitro* data, we tested lymphangiogenesis in physiologically relevant models. First, we used *ex vivo* rat mesentery tissue (*14*) to analyze impact of treatment on lymphatics within intact vascular networks (**Fig. 2A**). Carboplatin significantly increased sprouting of lymphatic vessels (**Fig. 2B-D**) but not blood vessels (**Fig. S2A-C**).

The importance of lymphatics in mammary carcinoma progression is well-established. We treated healthy, non-tumor-bearing female mice with 0-3 doses of carboplatin (8 mg/kg/dose) to examine lymphangiogenesis in naïve mammary fat pads (MFP) (**Fig. S3A-D**), histologically quantifying lymphatic vessel density (LVD), area, and perimeter (**Fig. S3E-F**). Carboplatin treatment resulted in significant dose-dependent increases in LVD in the MFP stroma of both Balb/c and SCID mice (**Fig. 2E, Fig. S3G**), but no significant increase in vessel area or perimeter (**Fig. S3G,H).** LVD remained elevated 8 weeks after final treatment with carboplatin comparable to that at day 3 (**Fig. 2F**).

Platinum chemotherapy is standard of care in high-grade serous ovarian cancer along with cytoreductive surgery. Because the omentum is the most frequent site of ovarian cancer metastasis, it is routinely removed during surgery, giving us access to histologically normal tissues. We analyzed lymphatics in omentum from patients treated with neoadjuvant carboplatin and docetaxel chemotherapy prior to surgery (**Table S4**). All omentum samples were pathologist-identified as uninvolved and ostensibly healthy.

Histologically normal omentum treated with carboplatin had significantly higher LVD compared to that of untreated patients (**Fig. 2G,H**). Though these tissues also received taxane treatment, previous findings have demonstrated that taxanes require tumor to promote lymphangiogenesis (*10*). Thus, the lymphangiogenic effects observed here are likely due to carboplatin, concordant with our results *in vitro* and in rodents.

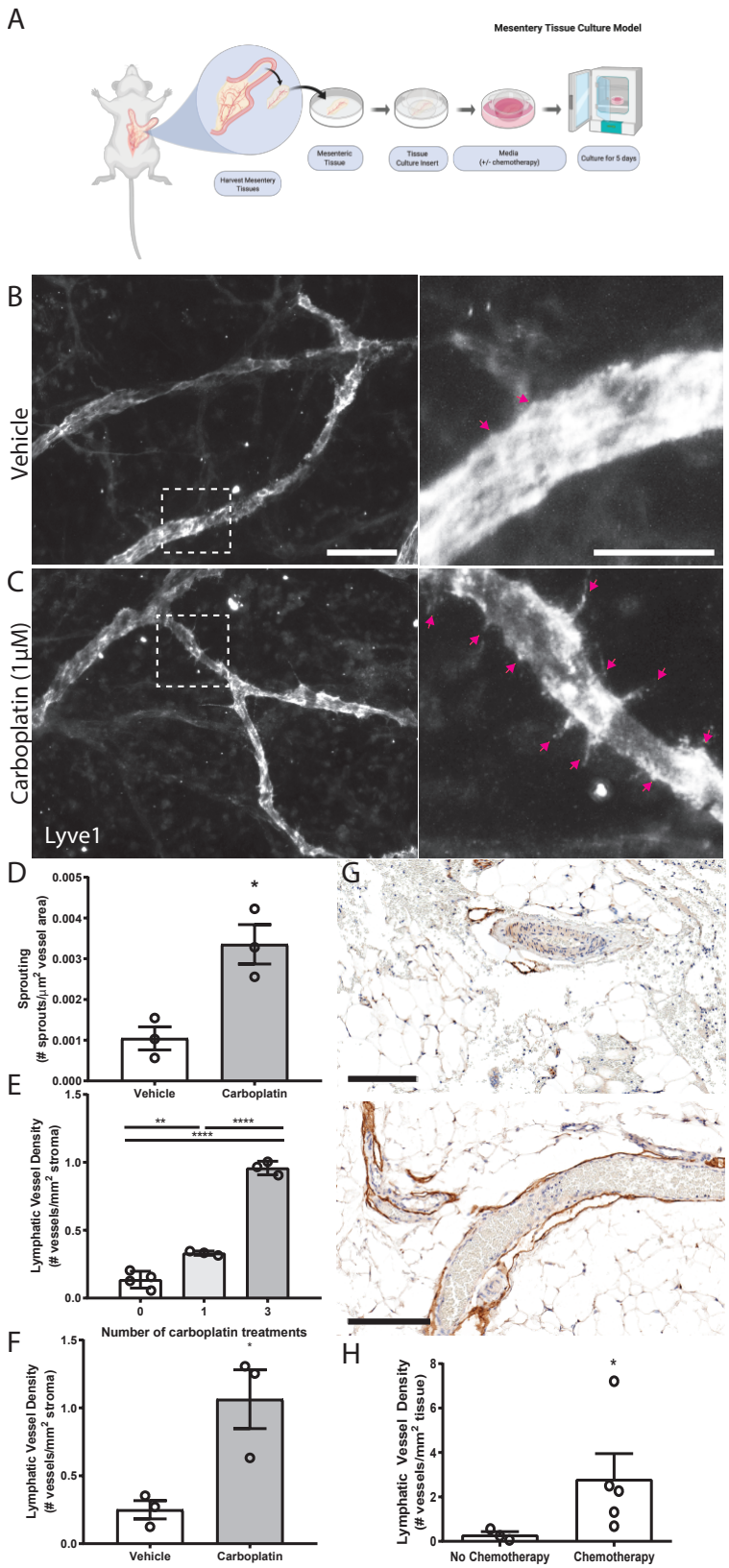

<u>Figure 2:</u> Carboplatin induces lymphangiogenesis in healthy tissues (A) Schematic of rat mesentery culture model. **(B)** Vehicle-treated lymphatic vessels from mesentery cultures stained with LYVE-1 (grey). (**i**) High magnification image of boxed area in **A**. (**C** Carboplatin-treated lymphatic vessels from mesentery cultures stained with LYVE-1 (grey).(**ii**) High magnification image of boxed area in **B**. Scale bar=100μm. **(D)** Number of sprouts per lymphatic vessel area. n≧3. **(E)** Lymphatic vessel density (podoplanin+ vessels per mm^2 stroma) in whole mammary fat pads of healthy mice treated with systemic carboplatin (8 mg/kg/dose) or vehicle by IV. n≧4. **(F)** Lymphatic vessel density measured in mammary fat pads of healthy mice 2 months after treatment with 3 doses of carboplatin or vehicle, n=3. **(G)** Representative images of lymphatic vessels in histologically benign omentum from patients treated with no chemotherapy (top) or neoadjuvant carboplatin combination chemotherapy (bottom) (*see Supplemental Table 4*) podoplanin (brown) and hematoxylin (blue). (**H**) Lymphatic vessel density in patient samples. Scale bar = 200 microns. N=8 patients. *p<0.05, **p<0.01, ****p<0.001.

Platinum chemotherapy induces lymphangiogenesis in ovarian and breast tumor stroma

In cancerous omental tissue from 17 patients with or without carbotaxol treatment prior to surgery (**Fig. 3A, Table S5**), we again detected a significant increase in LVD in patients receiving neoadjuvant platinums (**Fig. 3B**). Similarly, in primary tumor stromal tissue from 27 TNBC patients (**Fig. 3C, Table S6**), there was a significant increase in LVD in patients treated with platinums prior to surgical resection (**Fig. 3D**). Therefore, neoadjuvant chemotherapy that includes platinum corresponds with increased lymphangiogenesis in the human tumor stroma.

While ovarian cancers can spread through multiple mechanisms, breast cancer preferentially metastasizes via lymphatics(*4*). Therefore, we employed a series of breast cancer mouse models to analyze platinum effects on tumor-associated lymphangiogenesis: orthotopic 4T1 syngeneic tumors (immune-competent); orthotopic MDAMB231 xenograft (immune-compromised); or the inducible autochthonous mammary tumor model, L-Stop-L-K-$KRas^{G12D}p53^{flx/flx}$-L-Stop-L-*Myristoylated p110α*-GFP (immune-competent), which more closely mimics the malignant transformation and progression in humans (*15*). Mice received carboplatin when tumors were palpable, and there were no difference in tumor size observed (**Fig. S4A**). Histological analysis (**Fig. 3E-H**, **Fig. S4B,C**) showed significantly increased LVD after three treatments of carboplatin (**Fig. 3I**). Unlike in naïve MFP, lymphatic vessel area and perimeter significantly increased in immunocompetent mice (**Fig. 3J, S4D**).

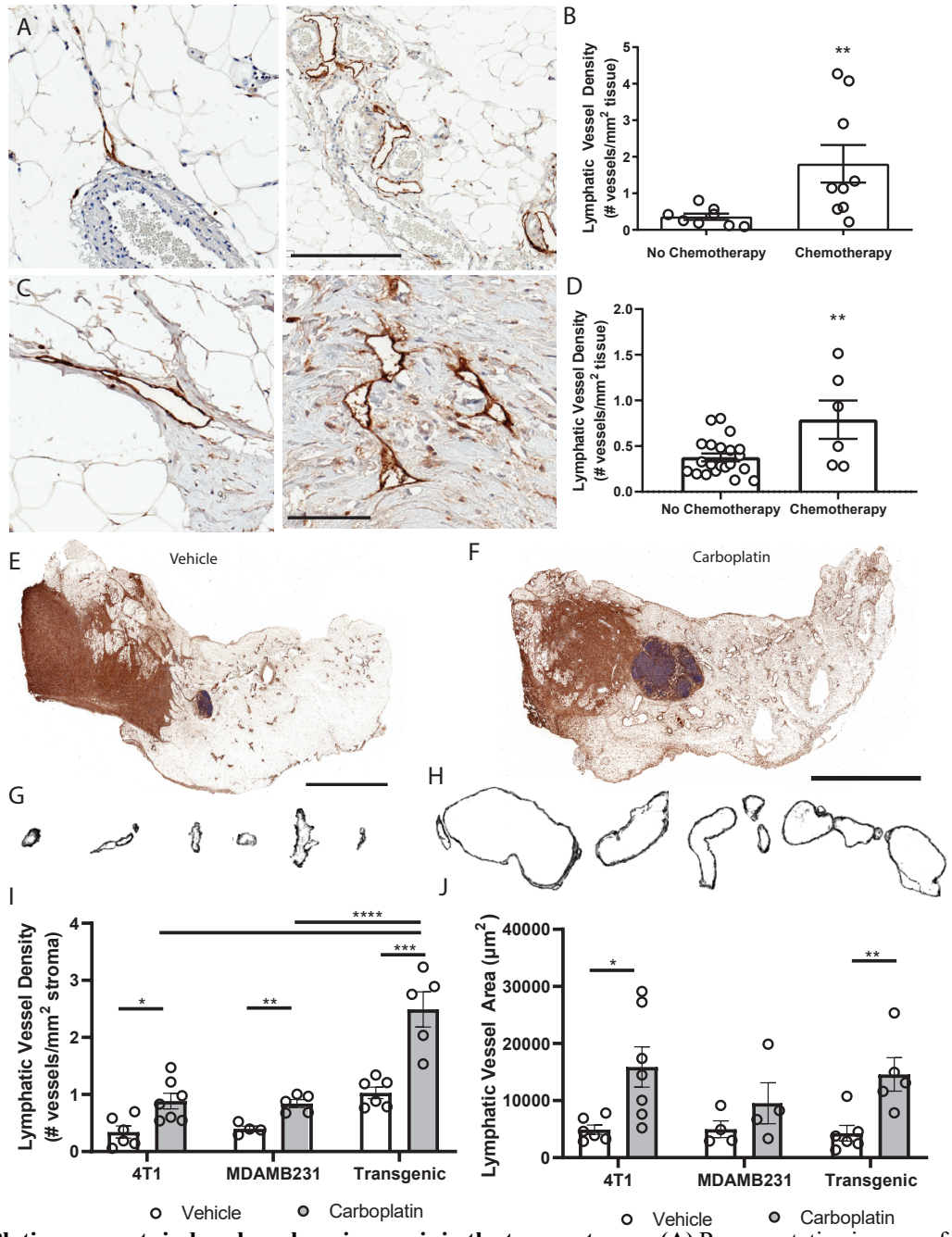

Figure 3: **Platinum agents induce lymphangiogenesis in the tumor stroma** **(A)** Representative images of tissues from ovarian cancer patients treated with no chemotherapy (*left*) or neoadjuvant carboplatin and paclitaxel (*right*) in cancerous omentum with podoplanin(brown) and hematoxylin(blue). (**B**) Quantified lymphatic vessel density (N= 17). **(C)** Representative images of tissues from triple negative breast cancer patients treated with no chemotherapy (*left*) or neoadjuvant platinum and taxane (*right*) with podoplanin(brown) and hematoxylin(blue). (**D**) Lymphatic vessel density (N=27) *p<0.05, **p<0.01, scale bar=200µm. **(E)** Representative tumor-bearing mammary fat pad with podoplanin (brown) and hematoxylin (blue) from vehicle-treated transgenic $Kras^{G120D}p53^{fl/fl}p110a^{myr}$ mice. **(F)** Representative whole tumor-bearing mammary fat pad from carboplatin-treated transgenic mice. (**G**) Representative individual lymphatic vessel cross-sections from **E**. (**H**) Isolated lymphatic vessels from **F**. (**I**) Lymphatic vessel density (lymphatic vessels per stromal area) in tumor-bearing mammary fat pads in 3 orthotopic mouse models of breast cancer (syngeneic 4T1, transgenic $Kras^{G120D}p53^{fl/fl}p110a^{myr}$, and xenografted MDA-MB-231). (**J**) Lymphatic vessel area (μm^2) mouse models of breast cancer as described in **I**. *p<0.05, **p<0.01, ***p<0.001, ****p<0.0001, n≥4/cohort.

Platinum-induced lymphangiogenesis primes the premetastatic niche for metastasis

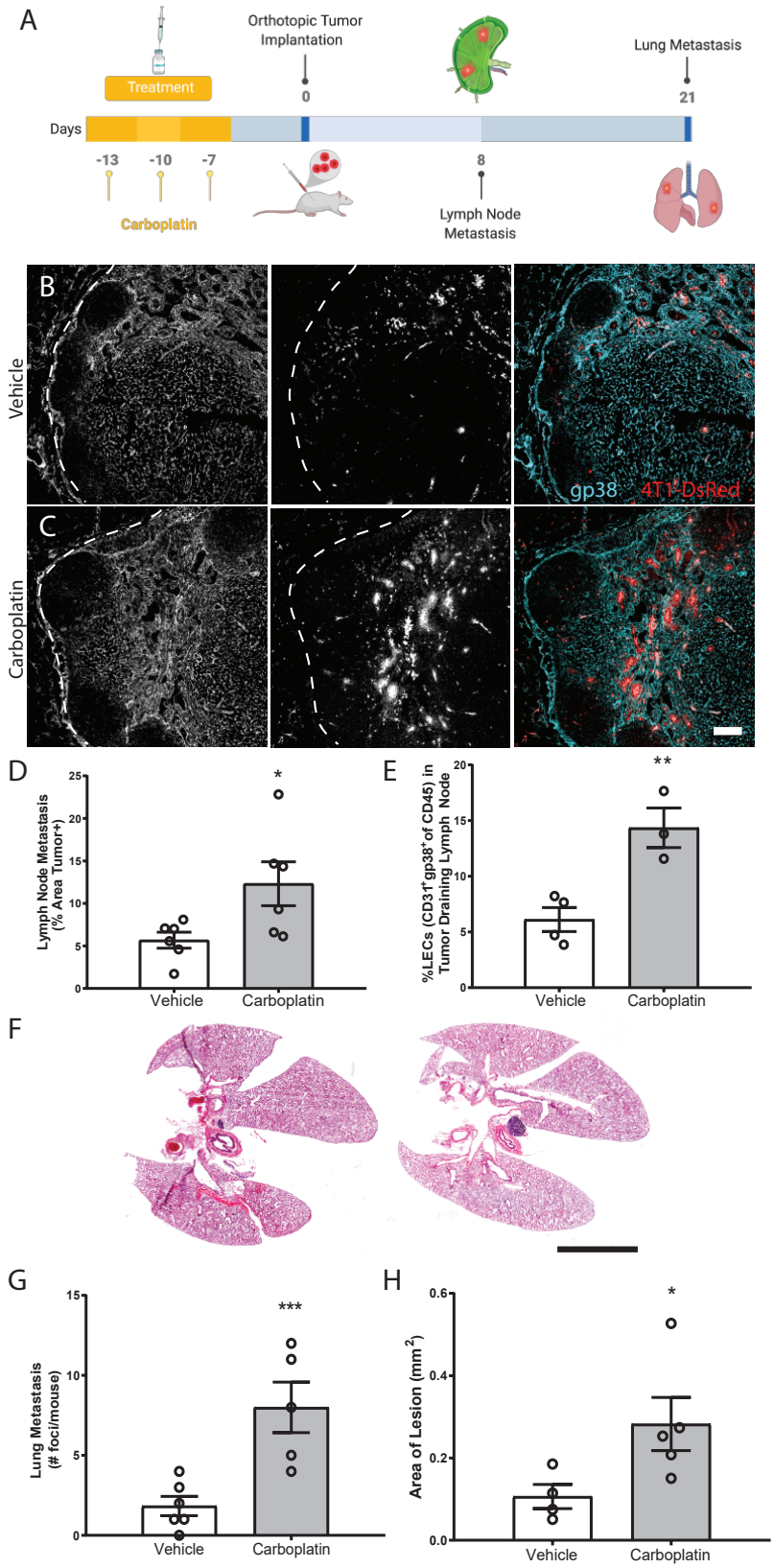

Enlargement and remodeling of lymphatic vessels is known to increase tumor cell dissemination (*6*, *8*, *16*) with LVD and tumor spread correlating in murine and human cancers (*17–19*). We hypothesized that priming of naïve tissues with carboplatin promotes tumor cell invasion and metastasis.

We treated healthy, tumor-naïve mice with systemic carboplatin to induce lymphangiogenesis (**Fig. 4A**), followed by orthotopic implantation of 4T1 tumor cells 1 week later. Though there was no

Figure 4: **Systemic priming with carboplatin increases metastatic spread of 4T1 breast tumors (A)** Experimental timeline for carboplatin pretreatment (8 mg/kg x 3 or vehicle) followed by 4T1 tumor implant and subsequent tissue harvest. **(B)** Representative images of 4T1 cells (red) in vehicle pretreated tumor-draining inguinal lymph nodes (TDLN) counterstained with podoplanin (cyan). (**C**) Representative images from carboplatin pretreated TDLNs. Scale bar=100µm. **(D)** Percentage of TDLN area covered by tumor cells as assessed by image thresholding in ImageJ. **(E)** Percent LECs of stromal cells in axillary TDLN after treatment as measured by flow cytometry. **(F)** Cross-section of lungs from vehicle (left) and carboplatin (right) -primed mice by H&E. Scale bar=1mm (**G**) Number of metastatic foci in lung per mouse. **(H)** Area of macroscopic metastatic lesions in lung. *p<0.05, ***p<0.005 as analyzed by individual *t* test, n≥4..

significant difference in tumor size at endpoints (**Fig. S5A**), tumor cell metastasis to the tumor-draining inguinal lymph node (TDLN), considered a first step in tumor cell dissemination (*4*), significantly increased in platinum pre-treated TDLNs compared to control (**Fig. 4B-D**). Platinum-pretreated TDLNs had significantly higher LEC populations with platinum pretreatment, indicating lymphangiogenesis (**Fig. 4E**). These data suggest that the lymphatics activated and remodeled by platinums are functionally capable of promoting metastasis. We also evaluated whether platinum-priming could contribute to distant metastases, e.g. to lung. 21 days after implantation, 100% of carboplatin pre-treated mice showed gross lung metastases, compared to 50% of the vehicle. Microscopic examination of lungs showed significantly increased numbers of foci (**Fig. 4G**) that were significantly larger with pretreatment (**Fig. 4H**). Therefore, priming tissues by carboplatin-induced lymphangiogenesis promotes LN and lung metastasis.

Carboplatin yields an inflamed lymph node phenotype with increased lymphangiogenesis

Lymphangiogenesis is considered a critical component of premetastatic niche formation, especially in the lymph node, a highly lymphovascularized organ ripe for metastatic colonization. Carboplatin treatment of LNs from tumor-naïve mice resulted in larger LNs with hyperplastic lymphatics and increased podoplanin staining (**Fig. 5A, Fig. S6A,B**), with a significant increase in LEC number (**Fig. 5B**). Each of these phenomena has been associated with LN inflammation and tumor metastasis (*20*).

The expansion of lymphatics led us to examine the relationship between LECs and the LN microenvironment with treatment. We also wanted to define the effects of platinum on other cell populations in the context of an intact lymph node. To do this, we used a unique *ex vivo* lymph node slice model (**Fig. 5C**) where each slice represents a distinct section of the lymph node with associated differences in cellular and extracellular composition. Representative slices from Prox1-GFP mice showed qualitative increases in lymphangiogenesis (**Fig. 5D**), though imaging-based quantification was difficult. Flow cytometry of cells from single slices confirmed that carboplatin treatment of slices significantly increased the LEC population but not the BEC, fibroblastic reticular cell, or T cell populations (**Fig. S6C-E**).

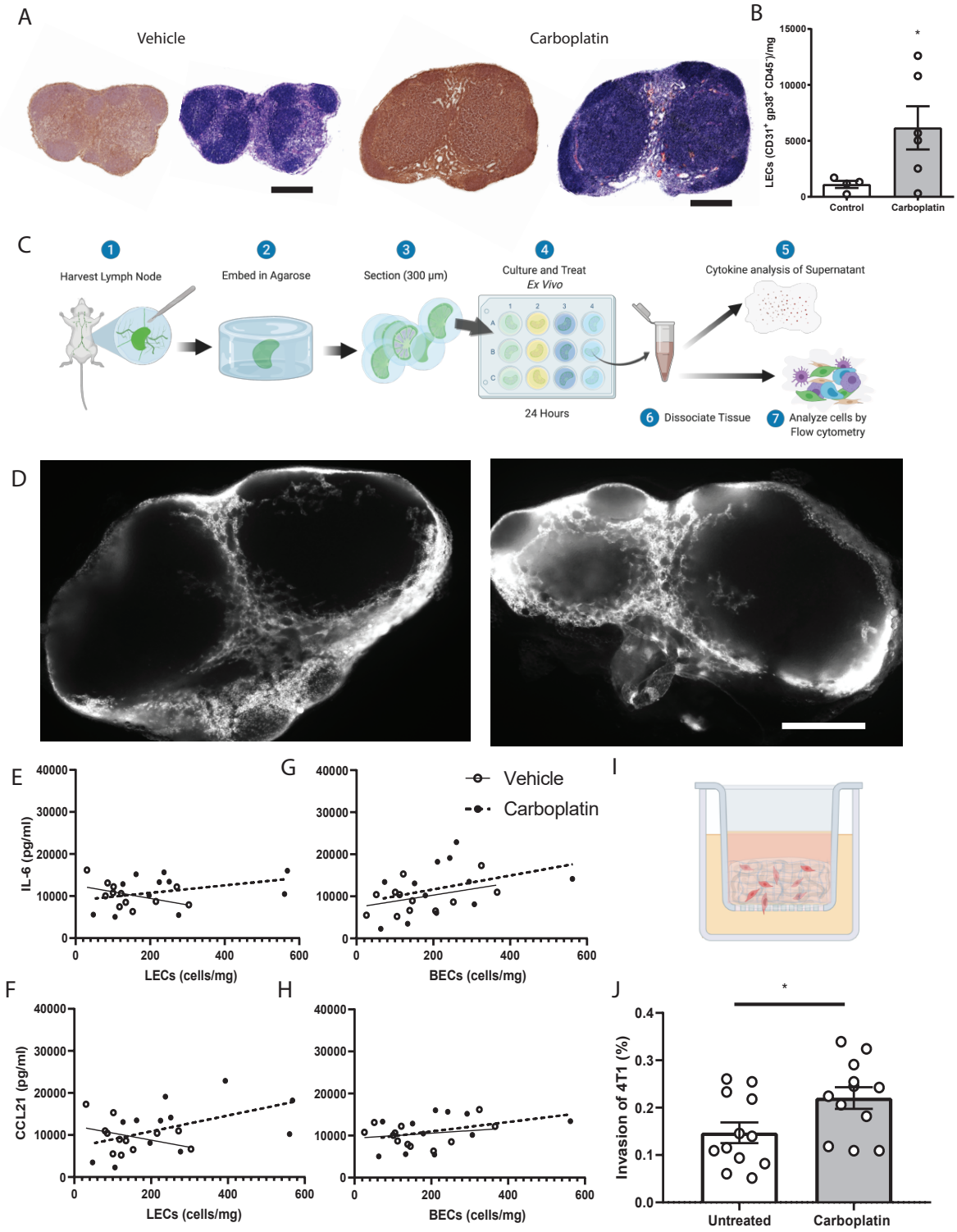

Figure 5: Carboplatin increases lymphatic endothelial cell expansion in lymph nodes correlating with microenvironmental changes **(A)** Lymph nodes from healthy, tumor-naïve mice treated with vehicle and stained with (*left*) podoplanin (brown) and hematoxylin (blue) or (*right*) H&E. **(B)** LEC number in vehicle-treated and carboplatin-treated lymph nodes *in vivo*. **(C)** Schematic of *ex vivo* lymph node slice model. **(D)** Lymph nodes from prox1-GFP tumor-naïve mice treated *ex vivo* vehicle (*left*) or carboplatin (*right*). Scale bar = 0.5mm **(E-H)** Correlations of cytokine/chemokine from supernatant of slices treated +/- carboplatin between: (**E**) IL6 v. LECs; **(G)** IL6 v. BECs; **(F)** CCL21 v. LECs; (**H**) CCL21 v. BECs. **(I)** Schematic of *in vitro* 4T1 3D invasion assay **(J).** Percent invasion of 4T1 cells toward treated lymph node slice supernatants (one point per slice). *p<0.05

In addition to providing more inlets and outlets for tumor cell dissemination, lymphangiogenesis can also increase metastasis through tumor-stimulating chemoattractants secreted by LECs. In a 3D tissue-engineered model of the lymphatic-stroma interface (*10*), carboplatin-exacerbated invasion of tumor cells was wholly dependent on LEC presence (**Fig. S5B,C**) indicating a chemotactic mechanism. In untreated slices, the number of LECs negatively correlated with the node's corresponding levels of IL-6 (r= -0.4533) (**Fig. 5E**) and CCL21 (r= -0.3673) (**Fig. 5F**). With carboplatin treatment, trends flipped, and LEC number positively correlated with IL-6 (r=0.3749) and CCL21 (r=0.4987). These cytokines weakly correlated with numbers of blood endothelial cells (BECs) with correlation trends remaining nearly identical with treatment (**Fig. 5G,H**). Other cytokines (TNFα, CXCL10) were weakly correlated with LECs but did flip with treatment (**Fig. S6F,G**). The number of T cells significantly correlated with the number of LECs in slices only when treated with carboplatin (r=0.6227, $p<0.05$) compared to vehicle (r=0.4179, p=0.176), potentially explaining, in part, the expansion of the lymph nodes seen *in vivo* (**Fig. S6H**). Collected carboplatin-treated slice supernatants elicited significantly more 4T1 invasion as compared to vehicle (**Fig. 5I,J**).

We hypothesized that priming also occurred in lung to promote chemotaxis similar to LN. As an *ex vivo* model of the lung was not readily available, we chose to treat healthy, tumor-free mice *in vivo* with carboplatin, similar to previous experiments, harvesting, digesting, and decellularizing lymph nodes and lungs three days after the final treatment (**Fig. S7**). Tumor cells invaded significantly more to carboplatin-treated lymph node (**Fig. 6A**) and lung (**Fig. 6B**) digested and decellularized tissues. These data suggest that platinum chemotherapy primes the premetastatic niche for subsequent tumor invasion.

Platinum-induced lymphangiogenesis and metastasis are inhibited through inhibition of VEGFR3

Having shown carboplatin treatment increases invasion and metastasis, we sought the underlying mechanism. VEGFR3 blockade reduces metastatic spread and lymphangiogenesis in a number of tumor models, as the VEGFC:VEGFR3 signaling pathway is one of the quintessential drivers of LEC proliferation(*6*). Our *in vitro* studies (**Fig. 1C,I**) led us to hypothesize that VEGFR3 is involved in

carboplatin-mediated lymphangiogenesis and metastasis. Thus we aimed to conduct our prior studies in the presence of anti-VEGFR3 blocking with an antibody or IgG control antibody.

In our prior invasion assay toward carboplatin-primed lungs/LN, addition of anti-VEGFR3 significantly attenuated platinum-induced invasion of 4T1 cells toward both tissue homogenates (**Fig. 6A,B**). In our *ex vivo* LN slice model (**Fig. 5C**), addition of anti-VEGFR3 significantly reduced the LEC numbers increased by carboplatin (**Fig. 6C**), with no effects on BECs (**Fig. S8A**). Corresponding reversal of chemokine secretion was seen (**Fig. S8B**). This data suggests that VEGFR3-activated LECs is directly responsible for platinum-induced priming of the premetastatic niche.

Ultimately, metastasis reduction *in vivo* is desired. Alternating carboplatin treatment with anti-VEGFR3 therapy (**Fig. S8C,D**) resulted in reversion of metastastic spread induced by carboplatin in $KRas^{G120D}p53^{fl/fl}p110\alpha^{myr}$ mice (**Fig. 6D,E**). Correspondingly, we could reverse carboplatin-mediated increases in LVD (**Fig. 3I**) in both 4T1 (**Fig. S8E**) and $KRas^{G120D}p53^{fl/fl}p110\alpha^{myr}$ **(Fig. 6F)** tumor-bearing fat pads**.** Similarly, blockade significantly reduced tumor-associated vessel area (**Fig. S8F,H**) and perimeter (**Fig. S8G,I)**. Moving to naïve tissues (**Fig. 2F**), anti-VEGFR3 reduced platinum-increased LVD in naïve MFPs (**Fig. 6G**), though the effect was stronger in tumor-bearing fat pads. Together, these data indicate that carboplatin-associated lymphangiogenesis occurs via a VEGFR3-dependent mechanism and therapeutic inhibition of this pathway is a viable solution to preventing these phenomena.

To loop back to our initial observations, we used MAZ51 (3-(4-Dimethylamino-naphthalen-1-ylmethylene)-1,3-dyhydro-indol-2-one), a specific small molecule inhibitor of VEGFR3, on monolayers of LECs. MAZ51 had little effect on LEC proliferation alone, but significantly suppressed carboplatin-induced LEC proliferation (**Fig. 6H**) and junctional disruption (**Fig. 6I)** to resemble untreated LECs (**Fig. 1**). Thus, VEGFR3 inhibition can directly revert the phenotypic effects of carboplatin seen *in vitro*, *ex vivo*, and *in vivo,* thereby explaining its therapeutic success.

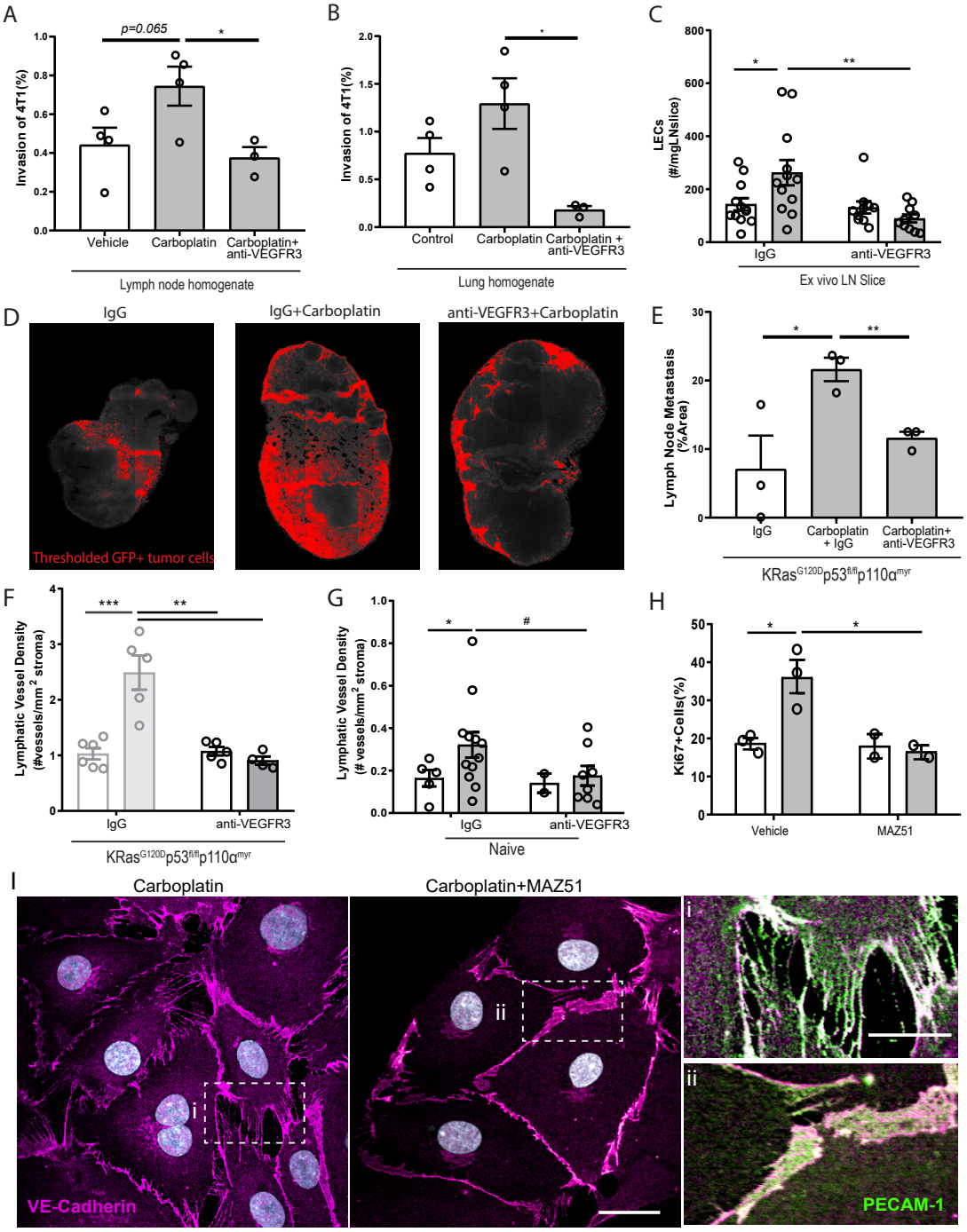

Figure 6: Blockade of VEGFR3 inhibits carboplatin-induced lymphangiogenesis and metastasis Invasion of 4T1 tumor cells towards digested and decellularized lymph node **(A)** and lung **(B)** from treated mice. **C)** Number of LECs in dissociated *ex vivo* lymph node slices after 24h treatment +/- carboplatin (1 μM) +/- anti-VEGFR3. **(D)** Representative thresholded images and **(E)** quantification GFP+ tumor cells in whole inguinal lymph nodes from KRas^{G120D}p53$^{fl/fl}$p110α^{myr} mice treated with vehicle/carboplatin and anti-VEGFR3/IgG. **(F)** Lymphatic vessel density (lymphatic vessels per stromal area) in tumor-bearing fat pad of KRas^{G120D}p53$^{fl/fl}$p110α^{myr} mice treated vehicle/carboplatin and anti-VEGFR3/IgG. Grayed bars represent data presented in previous figure but included here as point of reference. **(G)** Lymphatic vessel density in naïve, tumor-free fat pads from mice treated with vehicle/carboplatin and anti-VEGFR3/ IgG. **(H)** Percent proliferating cells per field by Ki67+ staining of human LEC monolayers treated *in vitro* with carboplatin (1 μM), VEGFR3 inhibitor MAZ51 (1 μM), or both for 6h. **(I)** LEC monolayers after 6h treatment VE-Cadherin (magenta) and PECAM1 (green) with high magnification images of boxed areas (I, ii) #p<0.1, *p<0.05, **p<0.01, ***p<0.001

Discussion

Here we see that platinum agents increase lymphatic expansion, proliferation, and expression of surface and secreted proteins, all of which are well-correlated with increases in tumor metastasis across a number of models (*6*). It is counterintuitive that chemotherapies would induce expansion of a cellular population and promote tumor progression, however, in fibroblasts, induction of stress responses by DNA-damaging chemotherapies can result in similar activation and compensatory proliferation (*21*, *22*). In addition to their well-known target of DNA, platinum chemotherapies have also been found to target cytoskeletal proteins, altering biological functions and potentially explaining our observed junctional changes (*23*). It has also been demonstrated that cisplatin can increase expression of VEGFR1 on VCAM1-expressing endothelial cells, though enhanced metastasis of primary tumor was not seen as we demonstrate here (*24*).

Lymphangiogenesis not only impacts tumor cells but also the stroma and immunity. Fluid drainage triggered by lymphangiogenesis can increase migration and trafficking of tumor cells, dendritic cells, and macrophages (*25*). Increased fluid flow activates fibroblasts yielding stromal collagen deposition and reorganization which can increase tumor cell invasion (*26*). LVD increased in both tumor and naïve fat pads while lymphatic vessel enlargement only occurred in tumor. It is possible that the increased fluid flow and cytokine production elicited by the tumor may exacerbate lymphatic dilation in this context (*6*, *8*, *16*). The proliferation of T-cells and LECs seen *ex vivo* may contribute to the lymph node growth seen *in vivo*, but cellular migration and infiltration from the tissue is likely more influential. The implications of lymphangiogenesis to tumor immunity is vast as lymphatics actively participate in tumor tolerance via numerous mechanisms, including a dependency on CCL21/CCR7 interactions (*27*, *28*). Therefore, increased LECs in lymph nodes after treatment could enhance tolerance in this metastatic organ, potentially dampening T cell responses, though we did not directly examine this. As platinum chemotherapy in some *in vitro* cases, can activate T cells, the consequences of increased tolerogenic LECs may interfere with this possible benefit (*23*). Conversely, lymphatics are critical in inflammation where increased cellular adhesion molecules, chemokine secretion, and permeability encourage lymphatic-immune interactions. While we did

not directly examine this in our studies, these phenomena promote the migration of immune cells such as macrophages and dendritic cells in inflammation and disease progression (*29*).

All therapies, anti-cancer or otherwise, eventually drain via our lymphatic system, but the majority of research has focused on the impacts of drugs on the blood vasculature, largely ignoring the impact on this endothelium (*30*). Research into specifically targeting lymphatics for treatment purposes is growing, without corresponding growth into how therapies directly affect the lymphatics themselves (*31*, *32*). Targeting of the lymph nodes with chemotherapy has been suggested as a potential treatment for metastatic spread (*33*). However, this study did not show efficacy, only an ability to target potential metastatic nodes. Though these strategies are not without merits, targeting of the lymphatic system and lymph nodes should be holistically studied in order to prevent inadvertent detrimental side effects as we highlight here. Indeed, more studies are emerging that suggest chemotherapy may paradoxically counteract its own efficacy through action on either the tumor cells or its associated stroma. Chemotherapies have myriad off-target effects, including enriching for cancer stem cell populations (*34*), promoting invasiveness (*35*), and inducing epithelial-to-mesenchymal transition (EMT) to encourage drug resistance (*36*). Last, ilation of vessels, as seen here, is associated with leakiness, and impaired pumping ability (*6*, *8*, *16*) indicating that there may be effects on other lymphatic malignancies, such as lymphedema. Regardless, off-target effects of these common cytotoxic agents certainly warrant further investigation.

Our studies describe a previously unknown pro-lymphangiogenic action of platinum chemotherapeutics that results in enhanced metastasis and reduced efficacy. These counter-therapeutic events are dependent on VEGFR3 and, therefore, supplementing chemotherapeutic regimens with anti-VEGFR3 was sufficient to prevent them. We believe that these findings highlight our incomplete understanding of chemotherapeutic action in the tissue stroma. Our data here suggest that informed pairing of chemotherapy with targeted therapies to the tumor microenvironment may improve overall efficacy, allowing chemotherapeutic cytoreductive benefits without unintended off-target effects that may lead to deadly recurrence. Specifically, we believe these studies may renew interest in the clinical potential of anti-VEGFR3 therapy, such as IMC-3C5 (*37*), which is well-tolerated, yet stalled in clinical trials, and may

show promising results when used in combination with specific chemotherapy within the proper disease context.

Materials and Methods

Cell culture

Human lymphatic endothelial cells (HMVEC-dLy, Lonza) were cultured in Endothelial Cell Growth Medium (EBM-2 basal media, Lonza) supplemented with recommended growth supplement kit (EGM-2MV BulletKit, Lonza). Mouse mammary carcinoma cell line 4T1-luc-red (generously given by the Cross laboratory at University of Virginia) originated from ATCC and were acquired from Perkin-Elmer (BW124087V) after lentiviral transduction of Red-FLuc luciferase gene. 4T1 cells were cultured in RPMI medium supplemented with 10% FBS. MDA-MB-231 were acquired from the ATCC and cultured in Dulbecco's modified Eagle's medium (DMEM, Gibco) and supplemented with 10% fetal bovine serum (FBS). All cell lines were grown sterilely in humidified atmosphere of 5% CO2 and 95% oxygen at 37°C. Cell lines were tested for mycoplasma and all experiments were completed afterwards.

In vitro drug treatment, immunocytochemistry, and live/dead assays

LECs were cultured on glass coverslips in complete media as described above; the LEC monolayer was treated with 1 μM carboplatin, cisplatin, oxaliplatin, docetaxel, doxorubicin, MAZ51(*38*), or appropriate solvent control (referred to as 'vehicle') for 6 hours (phenotypic studies) or 48 hours (live/dead analysis). After treatment, coverslips were fixed with 4% paraformaldehyde (PFA) for 30 minutes at room temperature and underwent immunofluorescent staining with Ki67 to assess proliferation (Millipore, Cat. #AB9260); ICAM1 to assess cellular adhesion molecule expression (Abcam, Cat. #AB2213); VE-Cadherin (Abcam, Cat. #AB33168) and CD31 (R&D systems, Cat. #AF806) to assess cellular junctions; p-VEGFR3 to assess activation of VEGFR3 signaling pathway (Cell Applications, Cat. #CY1115). For live/dead analysis, amine-based fixable live/dead solutions (Life Technologies, Cat. #L23101) were added to cell media of living LECs after 48 hours of drug treatment and five random images were taken of each well;

technical replicates were averaged to yield one biological replicate. Each quantification was performed with a minimum of 3 biological replicates.

Microarray and Gene Set Enrichment Analysis

Human LECs were treated *in vitro* with 1 μM carboplatin for 4 hours. Cells were lysed with RLT buffer and RNA was isolated using the QIAGEN RNeasy Kit (Cat #74104). Microarray was performed by the UVA DNA Sciences core using the Human Affymetrix GeneChip Array ([HuGene-2_1-st] Affymetrix Human Gene 2.1 ST Array). Gene lists were generated from microarray data corresponding to genes >1.25 LogFC and <0.75 logFC were used in downstream analyses. Differential targets identified were further subjected to gene set enrichment analysis performed using the ShinyGO enrichment tool using the STRING api. The STRING database (Search Tool for the Retrieval of Interacting Genes/Proteins) is a tool for looking at functional associations between different proteins(*39*). Protein-protein interactions are mapped across several curated databases and functional association is mapped in interaction networks. Gene interactions are then mapped to the KEGG pathway annotations with the adjusted p values representing pathway enrichment analysis from KEGG Release 86.1. MicroRNAs upregulated by >2 LogFC after treatment were subjected to enrichment analysis by DIANA mirPath v.3 from KEGG pathways significantly enriched with the union of target genes(*40*).

Reverse-phase protein array and pathway analysis

Human LECs were treated *in vitro* with 1 μM carboplatin for 6 hours. Cells were washed and lysed using RIPA buffer with protease and phosphatase inhibitors. RPPA was performed by the MD Anderson Functional Proteomics Core Facility as previously published(*41*). To assess which proteins reacted to the treatment, ratios of brightness were calculated and the distribution was assessed. Outlier proteins, for which the ratio was more than 2 standard deviations from the mean of the ratio distribution, were taken to be most affected by the treatment. Pathway enrichment analysis for these proteins was performed using

ConsensusPathDB (*42*) online tool and pathways enriched with statistical significance of unadjusted p-value of 0.01 were retained for further analysis.

Harvest, treatment, and whole mounting of *ex vivo* rat mesentery tissues

Mesentery tissues were harvested from rats as previously described by Azimi, et al(*14*, *43*) (**Fig. 2A**). Briefly, mesenteric tissue was harvested from the small intestine of an adult Wistar rat and transferred into a culture dish. Tissues were arranged on permeable membranes of cell crown inserts and cultured in MEM with 20% FBS and 1% penicillin/streptomycin for five days as previously described with 1 μM carboplatin or vehicle control. Tissues were then removed from inserts, grossed, mounted to slides, and fixed with methanol to undergo immunofluorescent staining with PECAM-1/CD-31 (BD Biosciences, Cat. #555026) for blood vessels and LYVE-1 (AngioBio Co., Cat. #11-034) for lymphatic vessels. Images were taken of a minimum of five random areas of vessel remodeling for each well and quantified by counting the number of sprouts normalized to vessel area in each field.

***In vivo* animal study design**

Studies in healthy, tumor-naive animals – 6-week-old female Balb/c mice were treated via tail vein injection of carboplatin unless otherwise noted. Mice underwent three total treatments with 8 mg/kg carboplatin or vehicle control (saline); each treatment was three days apart and mice were euthanized CO_2 inhalation three days following the final treatment. Naïve mammary fat pads and axillary lymph nodes were harvested; fat pads were post-fixed in 4% PFA for 24 hours, dehydrated, paraffin-embedded, and sectioned at 7-micron thickness to undergo immunohistrochemical staining (see Immunohistochemistry). Axillary lymph nodes were digested (dissociation as previously described(*44*)) and total LEC counts quantified (see Flow Cytometry).

Studies in 4T1 breast cancer model – 4T1 mouse mammary carcinoma cells were cultured as described above. 4T1 cells were suspended in 3.3 mg/ml growth-factor reduced basement membrane extract (Cultrex)

in phosphate-buffered saline (PBS) and orthotopically injected in a subareolar fashion into the fourth mammary fat pad of female balb/c mice. For most experiments, 50,000 4T1 cells were injected and mice treated with either 1 or 3 doses of 8 mg/kg carboplatin or vehicle by tail vein injection staggered by one day with anti-VEGFR3 antibody (100 μg per injection x 3 total injections, I.P., eBioscience (now ThermoFisher), Control IgG: rat monoclonal IgG2a kappa Isotype Control, Cat.#16-4321-85; Anti-VEGFR3: rat monoclonal IgG2a kappa to mouse VEGFR3 (AFL4): Cat. #16-5988-85) or IgG control antibody after tumors were just palpable. Mice were euthanized by CO_2 inhalation once tumors reached desired endpoints as assessed by caliper measurement. Tumor-bearing and contralateral naïve fat pads containing inguinal lymph nodes were harvested and post-fixed (24 h for naïve tissues, 48 h for tumors) in 4% PFA and processed for histology as described above; tumor-draining axillary lymph nodes were dissociated for flow cytometric analysis for LEC number.

For **priming experiments**, naïve mice were treated with three rounds of carboplatin as previously described and drug was allowed one week to clear(*45*). 10,000 4T1 cells were then injected as described above and allowed to grow until desired size endpoints were reached. Tumor-bearing fat pads were harvested and processed as described above. Lungs were removed, washed in saline, and fixed in 4% PFA for 48 h where they were then embedded in OCT and cryosectioned to undergo histological staining to examine metastasis.

Studies in transgenic breast cancer model – L-Stop-L-*KRas*^{G12D}*p53*$^{flx/flx}$L-Stop-L-*Myristoylated p110α*–GFP^{+} mice on a C57BL/6 background were generously provided by Melanie Rutkowski, University of Virginia. Mammary tumors were initiated by intraductal injection of adenovirus-Cre in these mice as previously described(*15*). Tumor growth was tracked via weekly caliper measurements. Once tumor growth became palpable, mice were randomized into groups with normalization of tumor size across groups, followed by the initiation of treatment. Animals were treated with 3 doses of IV carboplatin (8 mg/kg) or vehicle staggered by one day with 3 doses of anti-VEGFR3 antibody (100 μg) or IgG control as described above once tumors were palpable. Mice were euthanized by CO_2 inhalation when largest tumors reached 2 cm in any direction; tumor-bearing and contralateral naïve fat pads were collected for histology as described above.

Studies in human xenograft breast cancer model – Human MDA-MB-231 breast cancer cells were cultured as described above. $1x10^6$ cells were suspended in 3.3 mg/ml growth-factor reduced matrigel in phosphate-buffered saline (PBS) and orthotopically injected in a subareolar fashion into the fourth mammary fat pad of immunocompromised female mice (NOD.CB17-Prkdcscid/J). Once tumors were palpable, carboplatin was administed in three injections as described above. Mice were euthanized by CO_2 inhalation one week following final treatment; tumor-bearing and contralateral naïve fat pads were processed for histology as described above.

Human tissue sample acquisition

Remnant, to be discarded, surgical resections (not needed for diagnostic purposes) of omental metastatic ovarian cancer and patient-matched normal omentum and benign pelvic mass omentum for immunohistochemical staining with podoplanin were collected into a tissue and data bank by waiver of consent and approved by the University of Virginia Institutional Review Board for Health Sciences Research. The UVA Biorepository and Tissue Research Facility procured remnant samples, including all breast cancer specimens and the majority of omental specimens, under this protocol from UVA Pathology for fixed and embedded specimens in paraffin. De-identified tissues and associated clinical data were pulled from this tissue bank and used in experiments approved by UVa IRB-HSR.

Immunohistochemistry

Tumor-bearing mammary fat pads and lung tissues were dissected from mice and post-fixed in 4% PFA for 48 hours at 4°C; naïve fat pads underwent 24 hours of fixation. Fat pads were transferred to 70% ethanol for 24 hours, dehydrated, and paraffin-embedded. Tissues were sectioned at 7 μm thickness. Sections were stained with anti-podoplanin antibody (1 μg/ml, R&D Systems) followed by ImmPRESS HRP anti-goat IgG peroxidase/SG peroxidase detection (Vector Labs) and nuclear counter-staining with hematoxylin (Vector Labs) was performed. Human samples were processed and stained similarly. Slides were scanned at 20X on an Aperio Scanscope. For quantification of lymphatic vessel size, a custom interactive MATLAB

(MathWorks) program utilizing the Image Processing Toolbox (MathWorks) was designed to identify and analyze lymphatic vessels. First, IHC images were binarized using an intensity threshold capable of isolating vessels with high specificity. Next, a flood-fill operation was used to uniformly fill the vessel area. These regions were then extracted for analysis. Vessels not captured or incompletely captured by the automated procedure were identified by user-drawn regions of interest (n=5/cohort, minimum of 20-30 representative vessels/cohort). Centroid coordinates, perimeter, and area was computed for each vessel. For lymphatic vessel density, all lymphatic (podoplanin+) vessels in the mammary fat pad were counted and vessel number was normalized to size of stromal area for each mouse to assess lymphatic vessel density as lymphatic vessel #/mm^2 stroma. Intratumoral lymphatic vessels were rare and not included in these analyses in animal models. For lymphatic metastasis, sections were stained with anti-GFP antibody (5 µg/ml, Thermo Fisher, RFP Tag Monoclonal Antibody RF5R) and whole node confocal scans were used to quantify percent metastatic area of total node via image thresholding in ImageJ. Lungs were cryopreserved and embedded in OCT following fixation, cryosectioned, and stained with hematoxylin and eosin (H&E) to detect metastasis. Macroscopic metastatic lesions were counted by eye, whereas whole 20X scans of lung tissue were taken to detect micrometastatic lesions. Area of macroscopic lesions were measured in ImageJ.

Ex Vivo **Lymph Node Culture and Treatment**

Lymph Node Harvest, Processing, and Culture

All animal work was approved by the Institutional Animal Care and Use Committee at the University of Virginia. Lymph nodes from female mice were collected and sliced as previously reported(*46*). Briefly inguinal, axial and brachial lymph nodes were collected from C57Bl/6 mice aged 6-8 wks (Jackson), embedded in 6% low melting point agarose (Lonza) and sliced on a vibratome (Leica VT1000s, USA). Slices were allowed to rest for 1 hour at 37 °C and 5% CO_2 in "complete RPMI": RPMI (Lonza, 16-167F) supplemented with 10 % FBS (VWR, Seradigm USDA approved, 89510-186) 1x L-glutamine (Gibco Life Technologies, 25030-081), 50 U/mL Pen/Strep (Gibco), 50 µM beta-mercaptoethanol (Gibco, 21985-023), 1 mM sodium pyruvate (Hyclone, GE USA), 1x non-essential amino acids (Hyclone, SH30598.01), and 20

mM HEPES (VWR, 97064-362). After 1 hour of culture slices were moved to a fresh 24-well plate and cultured in complete RPMI and treated with either 1 μM Carboplatin (Tocris, UK) or vehicle control (1x PBS) in the presence of 1 μg/mL of either α-VEGFR3 (clone: AFL4, eBioscience USA) or IgG2aκ Isotype control (clone: eBR2a, eBioscience USA). Slices were cultured at 37 °C with 5% CO_2 for 24 hours. At 24 hours the media was removed for further analysis and replaced with fresh complete RPMI media.

Digestion and Cell Isolation

Digestion buffers I and II were made using a digestion media composed of Dulbecco's modified Eagle medium (1X, Gibco, 11965-092), 1% Penicillin Streptomycin (Gibco, 15140-122), 1.2 mM $CaCl_2$ (Fisher Scientific, BP510-500), and 2% fetal bovine serum (Sigma-Aldrich, F2442- 500mL). Lymph node slices were collected 24 hours after treatment with carboplatin, anti-VEGFR-3, or a combination of both. Slices were weighed, transferred to 5mL capped tubes containing digestion media, collagenase IV (1mg/mL; Gibco, 17104-019) and DNAse I (40ug/mL; Sigma-Aldrich, 10104159001), and incubated for 30 min at 37°C on a shaker. Supernatants were collected and set aside for downstream analysis of CD45+ cells. Digestion buffer II containing digestion media, collagenase D (3.3mg/mL; Sigma-Aldrich, 11088882001), and DNAse I (40ug/mL; Sigma-Aldrich, 10104159001), was added to the slices. Samples were incubated for 5 min at 37°C on a shaker, followed by manual pipetting and an additional 10 min at 37°C on a shaker. Tissues were then mechanically dissociated into a single-cell suspension by vigorous pipetting and passage through a 70um filter to obtain a single cell suspension of stromal populations.

Flow Cytometry

Stromal cell composition was assessed by flow cytometry. Single-cell suspensions were stained with Zombie Aqua viability dye (1:500, Biolegend, cat. #423102) to assess live vs dead cells, and Fc receptors were then blocked using anti-CD16/32 (1:100, Biolegend, cat. #101302). Single cell suspensions were subsequently stained with the following anti-mouse antibodies: CD45 (1:200, Biolegend, cat. #103151), CD31 (1:200, eBioscience, cat. #11-0311-82), and gp38 (1:200, Biolegend, cat. #127418). Cells were then fixed with the Cytofix/Cytoperm kit (BD Biosciences, cat. #554714) from BD Biosciences and stained

intracellularly for TGF-beta using anti-mouse LAP (1:100, Biolegend, cat. #141404). Data was collected on a Thermo Fisher Scientific Attune NxT cytometer and analyzed using FlowJo software.

Luminex Analysis

A specialized premixed multiplex kit (R&D Systems, lot: LXSAMSM-4) was formulated to examine murine CCL21/6Ckine (BR72), IL-6 (BR27), CXCL10/IP-10 (BR37) and TNF-alpha (BR14). Supernatant samples were tested using the MAGPIX System instrument (Luminex Corporation, Austin, TX). Cytokine concentrations were evaluated through Xponent software (Luminex Corporation). Samples were diluted 1:2 per manufacturer's instructions.

3D *in vitro* co-culture model

10,000 LECs were seeded on the underside of 8 μm pore size 96-well tissue culture inserts (Corning). After 48 h, 50 μl of a Rat Tail Collagen I (Corning)/basement membrane extract (Trevigen) (0.18 mg/ml Collagen, 0.5 mg/ ml BME) containing Cell Tracker dye (ThermoFisher). Labeled human mammary fibroblasts (100,000 HMF/ml) and human breast cancer cells (660,000 TNBC cells/ml) was placed atop the inserts. After gelation, media was added to the bottom compartment and flow was applied via a pressure head in the top compartment overnight (~ 1 μm/s; 16-18 h), after which point carboplatin was applied via flow to the top compartment for 24 h and then flushed from the system with basal media. 48 h after drug application, inserts were processed for invasion analysis (*10*, *47*). All experimental conditions were run as triplicate samples in individual inserts.

Invasion Assays

Tissue engineered 3D model of human breast tumor microenvironment: After gel was removed, tissue culture inserts were washed briefly in phosphate-buffered saline (PBS) and fixed with 4% paraformaldehyde. Inserts were stained with DAPI and visualized by fluorescence microscopy. Cancer cells (DAPI + Cell Tracker Deep Red+) were counted in five individual fields per well. Percent cancer cell

invasion was calculated as previously described. Three technical replicates were averaged for each experimental run to give a single biological replicate value for statistical analysis.

Ex vivo lymph node supernatants: For invasion assays, 100,000 4T1 cells were resuspended in a 1.8 mg/ml collagen I (rat tail collagen, Corning), 0.2 mg/ml basement membrane extract (reduced growth factor, Trevigen) matrix which were loaded into a 96-well tissue culture insert plate (Corning). Supernatants were placed in the lower chamber and cells invaded for 18h before gels were removed. Membranes were fixed and stained with DAPI and cells quantified to calculate total percent invasion based on total cells counted/total cells seeded.

Tissue homogenates from treated mice: Tissues from mice treated with 3 doses of carboplatin (as described above) were perfused with saline and dissected out. These tissues were degraded using 0.1 mg/ml Liberase TM for 30 minutes at 37C and then centrifuged down. The supernatant was removed and snap frozen until use. These samples were analyzed using BCA assay (Pierce) to determine total protein content. For the invasion assay of 4T1 cells (as above with lymph node slice supernatants) 25µg was added to the lower well.

Flow Cytometry on *In Vivo* Tissues

Cells from *in vivo* digested lymph nodes and lungs were dissociated as previously described and stained with live/dead reactive dye, anti-mouse CD45 PerCP-Cy5.5 (eBioscience), anti-mouse CD31 FITC (eBioscience), and anti-mouse gp38 PE-Cy7 (eBioscience). Flow cytometry samples were processed using the Millipore Guava easyCyte 8HT Flow Cytometer and analyzed using InCyte software for total LEC counts per mg as well as percentage of LECs. Gating was done first on live cells, followed by CD45- populations. This subpopulation was gated for gp38 and CD31 with the following populations: CD31+gp38+ (LECs); CD31+gp38-(blood endothelial cells), and CD31-gp38+(fibroblastic reticular cells).

Statistical Analysis

All data are presented as mean ± standard error of the mean (SEM). One-way or two-way ANOVA followed by Tukey's multiple comparison test was used for statistical analysis of unmatched groups. Two group comparisons of normally distributed data as assessed by QQ plots were performed using unpaired t tests (with Welch's correction if standard deviations were unequal), while comparisons of non-normal data were performed using Mann-Whitney U tests. Statistical analyses were run using Graphpad Prism software. $p<0.05$ is considered statistically significant. All *in vitro* assays were performed with a minimum of three biological replicates unless otherwise noted, murine study numbers are noted in legends and by individual graphed data points. Graphs were generated using Graphpad Prism software and are shown with mean +/- standard error.

Figure Generation

Figures were generated using Adobe Creative Suite (Photoshop and Illustrator). Schematics were generated using BioRender.

References

1. B. A. Chabner, T. G. Roberts, Chemotherapy and the war on cancer. *Nat. Rev. Cancer*. **5** (2005), pp. 65–72.
2. O. Scully, B. Bay, G. Yip, Y. Yu, Breast Cancer Metastasis. *Cancer Genomics Proteomics*. **9**, 311–320 (2012).
3. U. H. Weidle, F. Birzele, G. Kollmorgen, R. Rueger, Mechanisms and Targets Involved in Dissemination of Ovarian Cancer. *Cancer Genomics Proteomics*. **13**, 407–423.
4. S. Y. Wong, R. O. Hynes, Lymphatic or Hematogenous Dissemination: How Does a Metastatic Tumor Cell Decide? (available at https://www.ncbi.nlm.nih.gov/pmc/articles/PMC1459485/pdf/nihms9707.pdf).
5. J. Lin, A. S. Lalani, T. C. Harding, M. Gonzalez, W.-W. Wu, B. Luan, G. H. Tu, K. Koprivnikar, M. J. Vanroey, Y. He, K. Alitalo, K. Jooss, Inhibition of Lymphogenous Metastasis Using Adeno-Associated Virus-Mediated Gene Transfer of a Soluble VEGFR-3 Decoy Receptor. *Cancer Res*. **65**, 6901–9 (2005).
6. S. a Stacker, S. P. Williams, T. Karnezis, R. Shayan, S. B. Fox, M. G. Achen, Lymphangiogenesis and lymphatic vessel remodelling in cancer. *Nat. Rev. Cancer*. **14**, 159–172 (2014).
7. E. Lee, E. J. Fertig, K. Jin, S. Sukumar, N. B. Pandey, A. S. Popel, Breast cancer cells condition lymphatic endothelial cells within pre-metastatic niches to promote metastasis. *Nat. Commun.* **5**, 1–16 (2014).
8. A. Christiansen, M. Detmar, Lymphangiogenesis and cancer. *Genes Cancer*. **2**, 1146–58 (2011).
9. D. Alishekevitz, S. Gingis-Velitski, O. Kaidar-Person, L. Gutter-Kapon, S. D. Scherer, Z. Raviv, E. Merquiol, Y. Ben-Nun, V. Miller, C. Rachman-Tzemah, M. Timaner, Y. Mumblat, N. Ilan, D. Loven, D. Hershkovitz, R. Satchi-Fainaro, G. Blum, J. P. Sleeman, I. Vlodavsky, Y. Shaked,

Macrophage-Induced Lymphangiogenesis and Metastasis following Paclitaxel Chemotherapy Is Regulated by VEGFR3. *Cell Rep.* **17**, 1344–1356 (2016).
10. A. R. Harris, M. J. Perez, J. M. Munson, Docetaxel facilitates lymphatic-tumor crosstalk to promote lymphangiogenesis and cancer progression. *BMC Cancer*. **18**, 1–16 (2018).
11. N. Howlader, A. Noone, M. Krapcho, D. Miller, A. Brest, M. Yu, J. Ruhl, Z. Tatlovich, A. Mariotto, D. Lewis, H. Chen, E. Feuer, K. Cronin, "SEER Cancer Statistics Review, 1975-2016" (Bethesda, 2019).
12. A. Alitalo, M. Detmar, Interaction of tumor cells and lymphatic vessels in cancer progression. *Oncogene*. **31**, 4499–4508 (2011).
13. D. O. Miteva, J. M. Rutkowski, J. B. Dixon, W. Kilarski, J. D. Shields, M. A. Swartz, Transmural Flow Modulates Cell and Fluid Transport Functions of Lymphatic Endothelium, doi:10.1161/CIRCRESAHA.109.207274.
14. M. S. Azimi, J. M. Motherwell, W. L. Murfee, An Ex Vivo Method for Time-Lapse Imaging of Cultured Rat Mesenteric Microvascular Networks HHS Public Access (2018), doi:10.3791/55183.
15. M. R. Rutkowski, M. J. Allegrezza, N. Svoronos, A. J. Tesone, T. L. Stephen, A. Perales-Puchalt, J. Nguyen, P. J. Zhang, S. N. Fiering, J. Tchou, J. R. Conejo-Garcia, Initiation of Metastatic Breast Carcinoma by Targeting of the Ductal Epithelium with Adenovirus-Cre: A Novel Transgenic Mouse Model of Breast Cancer Video Link. *J. Vis. Exp*, 511713791–51171 (2014).
16. Y. He, I. Rajantie, K. Pajusola, M. Jeltsch, T. Holopainen, S. Yla-Herttuala, T. Harding, K. Jooss, T. Takahashi, K. Alitalo, Vascular Endothelial Cell Growth Factor Receptor 3-Mediated Activation of Lymphatic Endothelium Is Crucial for Tumor Cell Entry and Spread via Lymphatic Vessels. *Cancer Res.* **65**, 4739–4746 (2005).
17. J. Wang, Y. Guo, B. Wang, J. Bi, K. Li, X. Liang, H. Chu, H. Jiang, Lymphatic microvessel density and vascular endothelial growth factor-C and -D as prognostic factors in breast cancer: a systematic review and meta-analysis of the literature. *Mol. Biol. Rep.*, 1–13 (2012).
18. V. Muralidharan, L. Nguyen, J. Banting, C. Christophi, The Prognostic Significance of Lymphatics in Colorectal Liver Metastases, doi:10.1155/2014/954604.
19. R.-C. Ji, Lymphatic endothelial cells, tumor lymphangiogenesis and metastasis: New insights into intratumoral and peritumoral lymphatics (2006), doi:10.1007/s10555-006-9026-y.
20. J. P. Sleeman, The lymph node pre-metastatic niche, doi:10.1007/s00109-015-1351-6.
21. Y. Sun, J. Campisi, C. Higano, T. M. Beer, P. Porter, I. Coleman, L. True, P. S. Nelson, Treatment-induced damage to the tumor microenvironment promotes prostate cancer therapy resistance through WNT16B. *Nat Med*. **18**, 1359–1368 (2012).
22. H.-S. Hsu, C.-C. Liu, J.-H. Lin, T.-W. Hsu, J.-W. Hsu, K. Su, Involvement of ER stress, PI3K/ AKT activation, and lung fibroblast proliferation in bleomycin-induced pulmonary fibrosis. *Sci. Rep.* **7** (2017), doi:10.1038/s41598-017-14612-5.
23. S. V Hato, A. Khong, I. Jolanda, M. De Vries, W. J. Lesterhuis, Molecular Pathways: The Immunogenic Effects of Platinum- Based Chemotherapeutics CME Staff Planners' Disclosures Learning Objectives. *Clin Cancer Res*. **20**, 2831–7.
24. L. G. M. Daenen, J. M. L. Roodhart, M. van Amersfoort, M. Dehnad, W. Roessingh, L. H. Ulfman, P. W. B. Derksen, E. E. Voest, Chemotherapy enhances metastasis formation via VEGFR-1-expressing endothelial cells. *Cancer Res.* **71**, 6976–85 (2011).
25. J. D. Shields, M. E. Fleury, C. Yong, A. A. Tomei, G. J. Randolph, M. A. Swartz, Autologous Chemotaxis as a Mechanism of Tumor Cell Homing to Lymphatics via Interstitial Flow and Autocrine CCR7 Signaling, doi:10.1016/j.ccr.2007.04.020.
26. A. C. Shieh, H. A. Rozansky, B. Hinz, M. A. Swartz, Tumor cell invasion is promoted by interstitial flow-induced matrix priming by stromal fibroblasts. *Cancer Res.* **71**, 790–800 (2011).
27. J. D. SHIELDS, Lymphatics: At the Interface of Immunity, Tolerance, and Tumor Metastasis. *Microcirculation*. **18**, 517–531 (2011).
28. A. Riedel, D. Shorthouse, L. Haas, B. A. Hall, J. Shields, Tumor-induced stromal reprogramming drives lymph node transformation. **17** (2016), doi:10.1038/ni.3492.

29. C. M. Card, S. S. Yu, M. A. Swartz, Emerging roles of lymphatic endothelium in regulating adaptive immunity. *J. Clin. Invest.* **124**, 943–952 (2014).
30. M. W. Dewhirst, T. W. Secomb, Transport of drugs from blood vessels to tumour tissue. *Nat. Rev. Cancer*. **17**, 738–750 (2017).
31. L. C. Dieterich, M. Detmar, Tumor lymphangiogenesis and new drug development. *Adv. Drug Deliv. Rev.* **99**, 148–160 (2016).
32. Y. Xie, T. R. Bagby, M. Cohen, M. L. Forrest, M. Edu, Drug delivery to the lymphatic system: importance in future cancer diagnosis and therapies. *Expert Opin Drug Deliv*. **6**, 785–792 (2009).
33. T. Kodama, D. Matsuki, A. Tada, K. Takeda, S. Mori, New concept for the prevention and treatment of metastatic lymph nodes using chemotherapy administered via the lymphatic network. *Sci. Rep.* **6**, 32506 (2016).
34. H. Lu, I. Chen, L. A. Shimoda, L. Tran, H. Zhang, G. L. Semenza Correspondence, Y. Park, C. Zhang, G. L. Semenza, Chemotherapy-Induced Ca 2+ Release Stimulates Breast Cancer Stem Cell Enrichment. *Cell Rep.* **18** (2017), doi:10.1016/j.celrep.2017.02.001.
35. L. Volk-Draper, K. Hall, C. Griggs, S. Rajput, P. Kohio, D. DeNardo, S. Ran, Paclitaxel therapy promotes breast cancer metastasis in a TLR4-dependent manner. *Cancer Res.* **74**, 5421–5434 (2014).
36. P. P. Shah, T. V Dupre, L. J. Siskind, L. J. Beverly, Common cytotoxic chemotherapeutics induce epithelial- mesenchymal transition (EMT) downstream of ER stress. *Oncotarget*. **8**, 22625–22639 (2017).
37. M. W. Saif, J. A. Knost, · E Gabriela Chiorean, S. Rama, P. Kambhampati, D. Yu, B. Pytowski, A. Qin, J. S. Kauh, B. H. O'neil, Phase 1 study of the anti-vascular endothelial growth factor receptor 3 monoclonal antibody LY3022856/IMC-3C5 in patients with advanced and refractory solid tumors and advanced colorectal cancer. *Cancer Chemother. Pharmacol.* **78**, 815–824 (2016).
38. V. Kirkin, W. Thiele, P. Baumann, R. Mazitschek, K. Rohde, G. Fellbrich, H. Weich, J. Waltenberger, A. Giannis, J. P. Sleeman, MAZ51, an indolinone that inhibits endothelial cell and tumor cell growth in vitro, suppresses tumor growth in vivo. *Int. J. Cancer*. **112**, 986–993 (2004).
39. D. Szklarczyk, A. Franceschini, S. Wyder, K. Forslund, D. Heller, J. Huerta-Cepas, M. Simonovic, A. Roth, A. Santos, K. P. Tsafou, M. Kuhn, P. Bork, L. J. Jensen, C. von Mering, STRING v10: protein-protein interaction networks, integrated over the tree of life. *Nucleic Acids Res.* **43**, D447-52 (2015).
40. I. S. Vlachos, K. Zagganas, M. D. Paraskevopoulou, G. Georgakilas, D. Karagkouni, T. Vergoulis, T. Dalamagas, A. G. Hatzigeorgiou, DIANA-miRPath v3.0: deciphering microRNA function with experimental support. *Web Serv. issue Publ. online*. **43** (2015), doi:10.1093/nar/gkv403.
41. R. Tibes, Y. Qiu, Y. Lu, B. Hennessy, M. Andreeff, G. B. Mills, S. M. Kornblau, Reverse phase protein array: validation of a novel proteomic technology and utility for analysis of primary leukemia specimens and hematopoietic stem cells. *Mol. Cancer Ther.* **5**, 2512–2521 (2006).
42. A. Kamburov, C. Wierling, H. Lehrach, R. Herwig, ConsensusPathDB--a database for integrating human functional interaction networks. *Nucleic Acids Res.* **37**, D623-8 (2009).
43. M. S. Azimi, M. Lacey, D. Mondal, W. L. Murfee, An Ex Vivo Tissue Culture Model for Anti-angiogenic Drug Testing. *Methods Mol. Biol.* **1464**, 85–95 (2016).
44. M. A. S. Broggi, M. Schmaler, N. Lagarde, S. W. Rossi, Isolation of Murine Lymph Node Stromal Cells. *J. Vis. Exp* (2014), doi:10.3791/51803.
45. Z. H. Siddik, D. R. Newell, F. E. Boxall, K. R. Harrap, The Comparative Pharmacokinetics of Carboplatin and Cisplatin in Mice and Rats. *Biochem. Pherntacoogy*. **36** (1987) (available at https://ac.els-cdn.com/0006295287904904/1-s2.0-0006295287904904-main.pdf?_tid=1b76d2c8-97bf-4cbe-a049-a19152578b00&acdnat=1530559274_4451939f22b13009935241a4cb47fff7).
46. B. D. Groff, A. W. L. Kinman, J. F. Woodroof, R. R. Pompano, Immunofluorescence staining of live lymph node tissue slices. *J. Immunol. Methods*. **464**, 119–125 (2019).
47. A. R. Harris, J. X. Yuan, J. M. Munson, Assessing multiparametric drug response in tissue engineered tumor microenvironment models. *Methods*. **134–135**, 20–31 (2018).

Acknowledgements: The authors would like to acknowledge AR Petrosky, DK Logsdon for technical assistance; JV Cross, D Gioeli, SP Verbridge, and JB Dixon for useful discussion; UVA Biotissue repository and research facility, flow cytometry core facility, advanced microscopy facility, and research histology facility. MD Anderson Cancer Center for RPPA Analysis.

Funding: Funding to JMM and MJP from the Kincaid Foundation and the UVA Cancer Center; ARH from the NIH Biotechnology Training Program, NIH 5 T32 GM008715; MJP from the NIH Cancer Training Program, NIH T32 CA 009109; MDACC RPPA funded by NCI #CA16672. Funding bodies did not participate in the collection, analysis, interpretation of data and writing of the manuscript. They provided the funds for the authors to conduct the study.

Author Contributions: Conceptualization, A.R.H., J.M.M.; investigation, A.R.H., M.S.A., F.N.A., M.B., S.E., M.J.P., C.B.R., R.B., R.C.C., K.T., J.M.M.; formal analysis, R.C., S.T., data curation, D.C.L., C.P., P.D., A.M., C.N.L., project administration, A.R.H., J.M.M., resources, S.P.C., C.N.L., R.R.P., M.R., J.M.M., software, A.M., R.C., S.T., J.S., validation, S.E., M.S.A., F.N.A., C.P., A.R.H., J.M.M.; visualization, A.R.H., R.C., S.E., J.M.M.; writing of original manuscript, A.R.H., J.M.M.; Review and editing of manuscript, M.R., R.R.P, and all authors.

Competing Interests: The authors have no competing interests to declare.

Supplementary Materials
Table S1 – S6
Fig. S1 – S8 (with legends)